Article

Ultralight Magnetic Nanofibrous GdPO₄ Aerogel

Matas Janulevicius, Vaidas Klimkevičius, Lina Mikoliunaite, Bonifacas Vengalis, Rokas Vargalis, Simas Sakirzanovas, Valentina Plausinaitiene, Albinas Zilinskas, and Arturas Katelnikovas*

Read Online

ACCESS | Metrics & More | Article Recommendations | Supporting Information

ABSTRACT: Anisotropic aerogels are promising bulk materials with a porous 3D structure, best known for their large surface area, low density, and extremely low thermal conductivity. Herein, we report the synthesis and some properties of ultralight magnetic nanofibrous GdPO₄ aerogels. Our proposed GdPO₄ aerogel synthesis route is eco-friendly and does not require any harsh precursors or conditions. The most common route for magnetic aerogel preparation is the introduction of magnetic nanoparticles into the structure during the synthesis procedure. However, the nanofibrous GdPO₄ aerogel reported in this work is magnetic by itself already and no additives are required. The hydrogel used for nanofibrous GdPO₄ aerogel preparation was synthesized via a hydrothermal route. The hydrogel was freeze-dried and heat-treated to induce a phase transformation from the nonmagnetic trigonal to magnetic monoclinic phase. Density of the obtained magnetic nanofibrous monoclinic GdPO₄ aerogel is only ca. 8 mg/cm³.
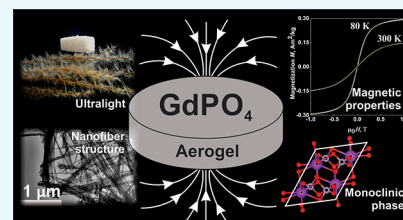
1. INTRODUCTION

An interest in synthesis and development of various rare-earth (RE)-based materials is consistently growing because of successful application of such materials in various high-tech and biomedical fields.[1−6] RE orthophosphates possess many beneficial features, such as high thermal (up to 2300 °C) and chemical stability, low solubility, and desirable optical properties [such as high refractive index (YPO₄ = 1.76, LaPO₄ = 1.85, and GdPO₄ = 1.97)].[7−9] Additionally, RE-based compounds are often referred as promising hosts for nuclear waste management.[10,11]

Aerogels are materials with a set of outstanding properties, such as extremely low density, large surface area, and low thermal conductivity. Despite a wide variety of materials that can be processed to very porous and low-density aerogel-like substances, there is still plenty room for specifically tailored and multifunctional systems. Aerogels can be prepared from a variety of different organic and inorganic substances, recent studies even report aerogels prepared from silver and gold.[12−14] Aerogel-based materials are considered for application in numerous fields ranging from tissue engineering and biosensing to catalysis and aerospace applications.[15−21] Introducing porosity in anisotropically structured magnetic materials would lead to the perfect supports for magnetic separations in biotechnology, environmental fields, or for magnetic field-assisted chemical reactions.[22−24] Typically, anisotropic aerogels are made from anisotropic particles (rods, fibers, wires, etc.), which are intertwined in all directions chaotically. The result of such chaotic interweaving of magnetic fibers is fully compensated overall magnetic momentum; therefore, magnetic properties of such an anisotropic aerogel would be significantly quenched.[25] Thus, obtaining a magnetic anisotropic aerogel as a homogeneous

system with magnetic properties still remains an enormous challenge. Most of the recent papers report magnetic aerogels as composite materials, where magnetic properties are introduced by incorporating magnetic nanoparticles into an originally nonmagnetic aerogel matrix.[26−29]

RE elements, in turn, can be used to bring a whole new class of aerogels. RE elements would enable us to obtain homogeneous aerogel platforms with both magnetic and optical properties. Such materials could also be used in designing novel composite-based aerogels as templates. For example, Gd³⁺-containing inorganic materials usually are magnetic because of the strong paramagnetic nature of Gd³⁺ ions.

Until now, there is only one scientific paper published on RE orthophosphate aerogels by Yorov et al., where the CePO₄ aerogel was successfully obtained and characterized.[30] However, the CePO₄ aerogel synthesis procedure, reported in this work, needed various organic solvents, was very time-consuming (more than 10 days), and required sophisticated supercritical drying in CO₂. Thus, the more environmentally friendly and time-effective synthesis route for RE phosphate aerogel preparation still needs to be developed. Additionally, to the best of our knowledge, there is no information describing synthesis or preparation of homogeneous anisotropically structured magnetic RE aerogels; therefore, such materials can be referred to as innovation.
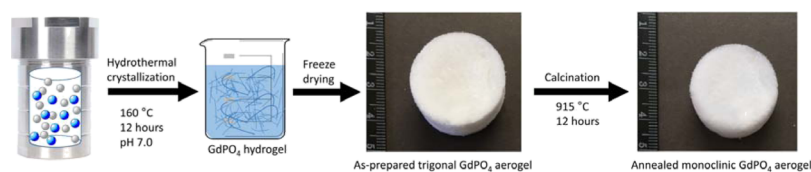
Figure 1. Preparation scheme for the as-prepared aerogel (trigonal phase) and annealed GdPO₄ aerogel (monoclinic phase).

The synthetic approach reported in this work can be applied to obtain various composite aerogels by simply incorporating different nanomaterials into the hydrogel, which further is used to produce aerogels. In such a way, gadolinium phosphate-based aerogels can be easily doped with other RE ions in order to tailor or enhance the desired properties.

In this work, we present the unique way for homogeneous fibrous magnetic GdPO₄ aerogel preparation. The method is simple, scalable, eco-friendly, and does not require any harsh precursors or conditions. The main characteristics of the synthesized nanofibrous GdPO₄ aerogel are also evaluated.

2. RESULTS AND DISCUSSION

The evolution of this research started by preparation of GdPO₄ nanoparticles with different morphologies via a hydrothermal synthesis route[31] at relatively high pH values and different Gd^{3+}/PO_4^{3-} ratios in the solution. Then, we observed that long and interwoven GdPO₄ nanofibers also can be obtained if pH of the synthesis solution is lowered to 7 and the Gd^{3+}/PO_4^{3-} ratio is fixed to 1 (Section S1 in the Supporting Information). Reducing the pH to 2 yields urchin-like microparticles, as shown in Figure S1a, whereas the increase in pH to 10 yields much shorter nanofibers (see Figure S1b); therefore, they cannot interweave sufficiently enough to form a hydrogel. The stirring should also be avoided because it breaks the delicate nanofibers (see Figure S1c). The synthesis at pH = 7 yielded a nearly transparent hydrogel with the final volume of 10 mL. We have also diluted this hydrogel to 20 and 30 mL before freeze-drying in order to check whether there is any influence to the aerogel formation. The best results were obtained for the 10 mL sample, where no anisotropic pore structures were detected. However, the samples with higher volume possessed the large anisotropic pores formed by ice crystals. This is supported by low-resolution scanning electron microscopy (SEM) images, as given in Figure S2. Moreover, if the samples were diluted to 30 mL, the aerogel structure collapsed during the freeze-drying procedure. The 10 mL volume hydrogel was washed and freeze-dried resulting in the "as-prepared" aerogel. Subsequently, this aerogel was annealed at 915 °C for 12 h in air in order to induce phase transformation from trigonal to monoclinic. The schematic representation of the synthesis process conducted to obtain GdPO₄ nanowires, hydrogel, and aerogel is provided in Figure 1.

Both, the as-prepared and annealed aerogels were investigated by powder X-ray diffraction (PXRD) to evaluate the phase composition and purity. The obtained XRD patterns for the as-prepared and annealed gadolinium phosphate aerogels are given in Figure 2a,b, respectively. XRD analysis reveals that the as-prepared GdPO₄ aerogel consists of the pure rhabdophane-type phase with the composition GdPO₄·nH₂O, which has trigonal lattice symmetry with the space group $P3_121$ (#152) (Figure 2a). In the rhabdophane structure, Gd^{3+} ions are 8-coordinated with oxygen ions. The resulting
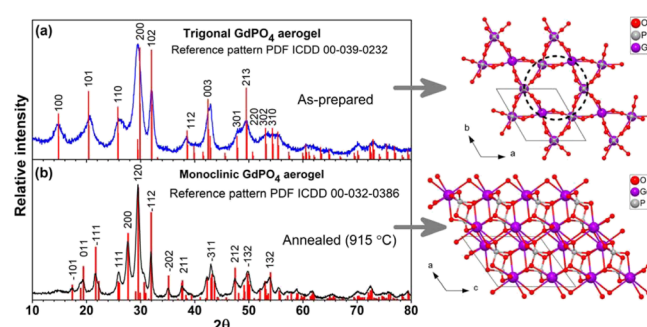
Figure 2. XRD patterns of the as-prepared (a) aerogel (trigonal phase) and annealed (b) GdPO₄ aerogel (monoclinic phase).

polyhedron, in turn, shares edges with four other GdO₈ polyhedrons and two PO₄ tetrahedra and vertexes with four PO₄ tetrahedrons. The visual representation of this building block is given in Figure S3. The lattice parameters of the as-prepared GdPO₄ aerogels were also calculated by applying the Le Bail method. The calculations yielded lattice parameters $a = 0.6935$ nm and $c = 0.6349$ nm, which are slightly larger than those reported in the reference structure GdPO₄·H₂O, PDF ICDD 00-039-0232 ($a = 0.69055$ nm, $c = 0.63257$ nm).

One-dimensional growth of the rhabdophane structure is well-known.[32] Anisotropic particles (nanorods) of various RE orthophosphates are the result of such an anisotropic growth and are reported in numerous papers and is characteristic structural feature of such compounds.[32−34] The crystalline structure of the trigonal rhabdophane phase contains zeolitic channels (pointed out by the black dashed circle in Figure 2a), which accommodate crystalline water, yielding GdPO₄·nH₂O stoichiometry. Water molecules, accommodated in zeolitic channels, go along the crystalline structure of anisotropic particles (in our case—nanofibers) or to be more exact, along the c-axis of the GdPO₄·nH₂O structure.[31] This crystalline water is responsible for stabilization of the trigonal phase. Therefore, loss of this crystalline water results in phase transformation to monoclinic.[35]

The anisotropic nature of lanthanide orthophosphates can be related to their crystal structure. From the thermodynamic point of view, the activation energy of growth on the ab-plane is lower in comparison with other crystal planes (ac and bc), implying that the ab-plane is the preferable plane for growth.[8] Similarly, Wang et al.[32] explain that different chemical potentials on different crystalline planes are responsible for the anisotropic growth rhabdophane phase crystals. According to the Thompson−Gibbs theory, chemical potential is directly proportional to the number of dangling bonds on the particular crystal plane.[36] Because the ab-plane (perpendicular to the c-axis) has the largest number of dangling bonds, this plane is preferable for further growth.

Annealing the as-prepared GdPO₄ aerogel results in phase transformation from trigonal (rhabdophane) to monoclinic (monazite) with a space group $P2_1/n$ (#14). The XRD pattern

shows that the pure $GdPO_4$ phase is obtained (see Figure 2b). In the monoclinic $GdPO_4$ structure, Gd^{3+} ions are nine-coordinated forming GdO_9 polyhedrons. Each GdO_9 polyhedron shares edges with six other GdO_9 polyhedrons and two PO_4 tetrahedra and vertexes with five PO_4 tetrahedrons.[37] The visual representation of this building block is given in Figure S4. Calculated lattice parameters for the annealed aerogel are as follows: $a = 0.6334$ nm, $b = 0.6854$ nm, $c = 0.6664$ nm, $\beta = 104.1°$, and are very similar to the ones provided in the ICCD database (PDF ICDD-00-032-0386 card) ($a = 0.63342$ nm, $b = 0.68451$ nm, $c = 0.66525$ nm, and $\beta = 104.0°$).

It is also necessary to mention that the monoclinic phase is more preferable as it possesses no crystalline water within its structure. The high content of crystalline water within the trigonal rhabdophane structure is known to quench luminescence emission significantly.[38,39] Therefore, such a monoclinic phase aerogel is much more suitable to be doped with RE ions to introduce luminescent properties. After annealing of the as-prepared aerogel at several temperatures, we found out that 915 °C is the highest temperature that the aerogel can withstand. Annealing at higher temperature resulted in collapse of the porous aerogel structure. Even samples annealed at 915 °C have already shown some signs of nanofiber melting, as demonstrated in transmission electron microscopy (TEM) images given in the Supporting Information Figure S5.

Furthermore, SEM and high-resolution TEM were used for morphological characterization of the as-prepared and annealed $GdPO_4$ aerogel samples. The obtained images are given in Figure 3. Several studies reported that during the
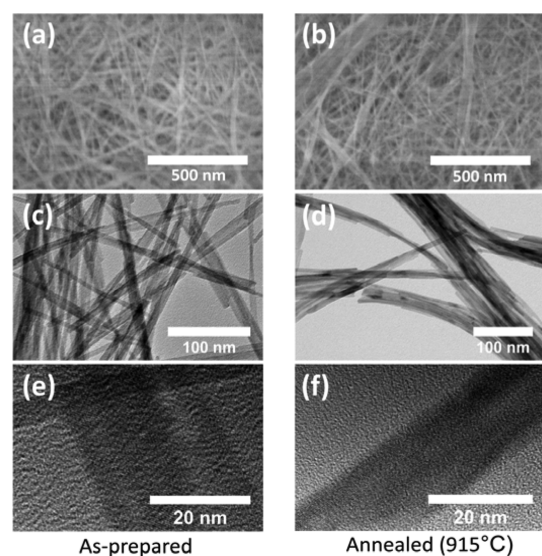
Figure 3. SEM and TEM images of the $GdPO_4$ aerogel: as-prepared trigonal (a,c,e) and annealed monoclinic (b,d,f).

annealing process at 900 °C temperature, when phase transformation occurs, anisotropic nanoparticles of trigonal $LnPO_4$ tend to deform and sinter badly.[38,40,41] This, however, is not true in our case, where virtually identical morphological features of both the as-prepared and annealed aerogel samples were observed. This can be evaluated from Figure 3. Both $GdPO_4$ aerogels are formed from high-aspect-ratio fibers; therefore, they can be regarded as anisotropic porous structures. High porosity of the structure ensures effective accessibility of the $GdPO_4$ aerogel surface throughout the

entire volume. SEM images also revealed that $GdPO_4$ nanofibers within an aerogel structure were randomly woven together, forming a three-dimensional (3D) nanofibrous network. It is necessary to emphasize again that a nanofibrous $GdPO_4$ aerogel withstands the annealing process and phase transformation, while maintaining the original 3D structure undeformed and undamaged.

The TEM images taken confirm the anisotropic nature of the nanofibrous structure of both the as-prepared and annealed $GdPO_4$ aerogels (see Figures 3c−f and S5). It is evident that fibers wider in diameter consist of axially agglomerated single crystalline nanofibers with a diameter ranging from 5 to 15 nm. TEM analysis of annealed samples has also confirmed that the annealing process causes significant changes in the morphology of nanofiber junctions—they become noticeably more agglomerated. Figure 3c demonstrates that prior to sintering, individual nanofibers were mostly separate throughout the junctions and contact areas. However, TEM images of the annealed aerogel (Figure 3d) show that nanofibers in contact places were more agglomerated and sintered, while in the as-prepared aerogel nanofibers were less affected by agglomeration. This is also supported by numerous TEM images given in Figure S6.

We have also evaluated the surface area and weight of the obtained $GdPO_4$ aerogels because these parameters are often referred to as the main characteristics defining aerogels. The as-prepared $GdPO_4$ aerogel had a density of around 10 mg/cm^3 and a specific surface area of around 29 m^2/g. On the contrary, the density of the annealed aerogel decreased even more, that is, to around 8 mg/cm^3, and the determined specific surface area was around 35 m^2/g. It is evident that the specific surface area of annealed $GdPO_4$ aerogels increases. Such an increase in the surface area is a result of crystalline water removal during the calcination step when the trigonal rhabdophane phase transforms to the monoclinic monazite phase. Because the total volume of the annealed aerogel virtually does not change, the weight loss results in the increased surface area.

Because the magnetic properties are the most interesting feature of the reported $GdPO_4$ aerogels, the magnetization measurements were performed in order to analyze magnetic behavior of the annealed $GdPO_4$ aerogel. Figure 4 shows magnetization versus applied field at $T = 300$ and 80 K of the sample containing randomly oriented fiber-like $GdPO_4$ nanocrystals. We point out the absence of any hysteresis either at
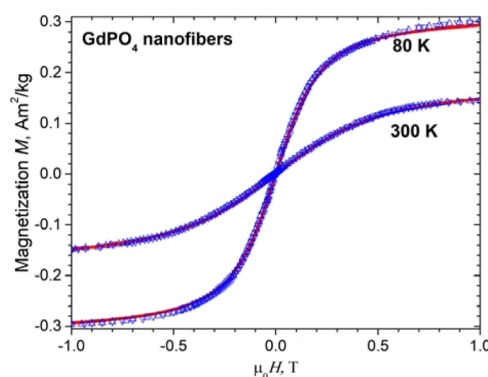
Figure 4. Mass magnetization vs magnetic field of the $GdPO_4$ nanotubes. Solid (red) lines show fitting of the experimental data by the Langevin function.

300 or 80 K temperature. The observed nonlinear (S-shaped) magnetization curves have been fitted well using a standard Langevin function[42] that is usually used to describe magnetization of superparamagnetic (SPM) systems

$$M(H, T) = NmL\left(\frac{\mu_0 mH}{k_B T}\right) \tag{1}$$

where N is the number of magnetic nanoparticles in the sample, m is the averaged magnetic moment of a particle, k_B is the Boltzmann's constant, and $L(x)$ is the Langevin function: $L(x) = \cot h(x) - 1/x$. The magnetic moment per nanoparticle of about 762 and 1190 Bohr magnetons at 300 and 80 K, respectively, was estimated in this work and corresponds to the best fitting of the magnetization curves with the Langevin function (see red solid curves in Figure 4). The observed nonlinear $M–H$ relation of the Langevin type and absence of hysteresis certify that the rod-like $GdPO_4$ nanofibers may be considered as a system of SPM particles. A similar nonlinear $M–H$ relation and absence of hysteresis both at RT and low temperatures have been reported earlier for the crystalline $GdPO_4$ material exhibiting the monoclinic crystalline structure and prepared in various forms, namely, polycrystals,[43] star-like nanocrystals,[44] and Tb- and Eu-doped nanotubes.[45,46] It is worth noting, however, that the room-temperature magnetization value, indicated in this work, is by factor 2−5 lower compared to those reported earlier. The observed magnetic properties of the nanotubes is a result of competing antiferromagnetic and ferromagnetic interaction of the paramagnetic Gd^{3+} ions with unpaired inner 4f electrons in the outer orbital in the monoclinic unit cell.[43] The reduced magnetization value at room temperature may probably be understood taking into account importance of the surface effects on magnetization of the nanocrystalline material and significant shape anisotropy of the rod-like nanocrystals.

3. CONCLUSIONS

In this work, we reported the synthesis and properties of the $GdPO_4$ aerogels composed of nanofiber-like crystals of a monoclinic phase, demonstrating chemical and thermal stability similar to that of a bulk material. Ultralight magnetic fibrous-structured $GdPO_4$ aerogels were prepared by a simple and eco-friendly aqueous hydrothermal synthesis method. The aerogel was produced by freeze-drying the hydrogel of $GdPO_4$ nanofibers, followed by a calcination step at 915 °C for 12 h. Various measurements were conducted to characterize the crystalline phase, structure, morphology, surface area, density, and magnetic properties. After the calcination step, the density of the aerogel decreased from ∼10 to ∼8 mg/cm^3. Morphological investigation revealed that both the as-prepared and annealed aerogels are highly anisotropic and possess a highly porous structure formed from the 3D network of overlapping $GdPO_4$ nanowires. The applied calcination step induced phase transformation from trigonal rhabdophane to monoclinic monazite.

One can expect that magnetic $GdPO_4$ aerogels (a promising platform for composite aerogels) are a very interesting class of novel materials because they offer magnetic properties, low density, and large surface area. These properties make $GdPO_4$ aerogels promising candidates in applications such as catalysts, nuclear waste management, electronic devices, neutron-absorbing materials, and so on.

We believe that fibrous, open-pore 3D-structured magnetic materials offer a flexible way for anisotropic texturing under a magnetic field. Magnetic RE orthophosphate-based aerogels offer a unique way for structuring because there is no need to introduce magnetic nanoparticles, leading to a homogeneous system. Finally, we enabled a relatively simple and fast route to obtain RE-based aerogels, which are yet emerging as a new class of materials.

4. METHODS

4.1. GdPO$_4$ Nanofiber Preparation. $GdPO_4$ nanofibers were prepared using an adopted procedure described in our previous publication with some minor adjustments.[31] The whole procedure in detail is provided in the Supporting Information Section S1. For the instrumental setup used for aerogel characterization, please see the Supporting Information Section S2.

4.2. GdPO$_4$ Aerogel Preparation. About 10 mL of the washed hydrogel was frozen in a freezer for 6 h at −24 °C. The frozen $GdPO_4$ hydrogel (containing $GdPO_4$ nanofibers) was then freeze-dried. As a result, a highly porous aerogel, composed of the 3D network of $GdPO_4$ nanofibers (with a diameter ranging from 5 to 15 nm), was obtained. This aerogel, hereafter, will be referred to as the "as-prepared". It should also be noted that the total volume of the as-prepared aerogel was virtually the same as the frozen $GdPO_4$ hydrogel, that is, ca. 10 mL. Finally, the as-prepared $GdPO_4$ aerogel was annealed at 915 °C for 12 h in order to induce phase transformation from trigonal to monoclinic.

■ ASSOCIATED CONTENT

Ⓢ Supporting Information

The Supporting Information is available free of charge at https://pubs.acs.org/doi/10.1021/acsomega.0c01980.

> $GdPO_4$ nanofiber preparation; instrumental setup; SEM images of particles obtained under different pH values; SEM images of aerogels obtained from different volumes of the hydrogel; building block in the trigonal rhabdophane $GdPO_4·H_2O$ structure; building block in the monoclinic monazite $GdPO_4$ structure; and TEM images (PDF)

■ AUTHOR INFORMATION

Corresponding Author

Arturas Katelnikovas − *Institute of Chemistry, Vilnius University, 03225 Vilnius, Lithuania;* ⓞ orcid.org/0000-0002-3295-8366; Email: arturas.katelnikovas@chf.vu.lt

Authors

Matas Janulevicius − *Institute of Chemistry, Vilnius University, 03225 Vilnius, Lithuania*

Vaidas Klimkevičius − *Institute of Chemistry, Vilnius University, 03225 Vilnius, Lithuania*

Lina Mikoliunaite − *Institute of Chemistry, Vilnius University, 03225 Vilnius, Lithuania; Center for Physical Sciences and Technology, 10223 Vilnius, Lithuania*

Bonifacas Vengalis − *Center for Physical Sciences and Technology, 10223 Vilnius, Lithuania*

Rokas Vargalis − *Institute of Chemistry, Vilnius University, 03225 Vilnius, Lithuania*

Simas Sakirzanovas − *Institute of Chemistry, Vilnius University, 03225 Vilnius, Lithuania*

Valentina Plausinaitiene − *Institute of Chemistry, Vilnius University, 03225 Vilnius, Lithuania*

Albinas Zilinskas − *Institute of Chemistry, Vilnius University, 03225 Vilnius, Lithuania*

Complete contact information is available at:
https://pubs.acs.org/10.1021/acsomega.0c01980

Author Contributions

The manuscript was written through contributions of all authors. All authors have given approval to the final version of the manuscript.

Notes

The authors declare no competing financial interest.

■ REFERENCES

(1) Huang, H.; Zhu, J.-J. The Electrochemical Applications of Rare Earth-Based Nanomaterials. *Analyst* **2019**, *144*, 6789−6811.

(2) Xu, C.; Qu, X. Cerium Oxide Nanoparticle: A Remarkably Versatile Rare Earth Nanomaterial for Biological Applications. *NPG Asia Mater.* **2014**, *6*, No. e90.

(3) Külah, E.; Marot, L.; Steiner, R.; Romanyuk, A.; Jung, T. A.; Wäckerlin, A.; Meyer, E. Surface Chemistry of Rare-Earth Oxide Surfaces at Ambient Conditions: Reactions with Water and Hydrocarbons. *Sci. Rep.* **2017**, *7*, 43369.

(4) Ignjatović, N. L.; Mančić, L.; Vuković, M.; Stojanović, Z.; Nikolić, M. G.; Škapin, S.; Jovanović, S.; Veselinović, L.; Uskoković, V.; Lazić, S.; et al. Rare-Earth (Gd^{3+},Yb^{3+}/Tm^{3+}, Eu^{3+}) Co-Doped Hydroxyapatite as Magnetic, up-Conversion and down-Conversion Materials for Multimodal Imaging. *Sci. Rep.* **2019**, *9*, 16305.

(5) Kong, T.; Zhang, C.; Gan, X.; Xiao, F.; Li, J.; Fu, Z.; Zhang, Z.; Zheng, H. Fast Transformation of a Rare-Earth Doped Luminescent Sub-Microcrystal via Plasmonic Nanoislands. *J. Mater. Chem. C* **2020**, *8*, 4338−4342.

(6) Sun, C.; Xue, D. Perspectives of Multiscale Rare Earth Crystal Materials. *CrystEngComm* **2019**, *21*, 1838−1852.

(7) Saltmarsh, N.; Kumar, G. A.; Kailasnath, M.; Shenoy, V.; Santhosh, C.; Sardar, D. K. Spectroscopic Characterizations of Er Doped $LaPO_4$ Submicron Phosphors Prepared by Homogeneous Precipitation Method. *Opt. Mater.* **2016**, *53*, 24−29.

(8) Fang, Y.-P.; Xu, A.-W.; Song, R.-Q.; Zhang, H.-X.; You, L.-P.; Yu, J. C.; Liu, H.-Q. Systematic Synthesis and Characterization of Single-Crystal Lanthanide Orthophosphate Nanowires. *J. Am. Chem. Soc.* **2003**, *125*, 16025−16034.

(9) Sun, C.; Xue, D. The Synergy Effect of Rare Earth Cations on Local Structure and PL Emission in a Ce^{3+}:$REPO_4$ (RE = La, Gd, Lu, Y) System. *Dalton Trans.* **2017**, *46*, 7888−7896.

(10) Terra, O.; Clavier, N.; Dacheux, N.; Podor, R. Preparation and Characterization of Lanthanum−Gadolinium Monazites as Ceramics for Radioactive Waste Storage. *New J. Chem.* **2003**, *27*, 957−967.

(11) Subramani, T.; Rafiuddin, M. R.; Shelyug, A.; Ushakov, S.; Mesbah, A.; Clavier, N.; Qin, D.; Szenknect, S.; Elkaim, E.; Dacheux, N.; et al. Synthesis, Crystal Structure, and Enthalpies of Formation of Churchite-Type $REPO_4 \cdot 2H_2O$ (RE = Gd to Lu) Materials. *Cryst. Growth Des.* **2019**, *19*, 4641−4649.

(12) Du, A.; Zhou, B.; Zhang, Z.; Shen, J. A Special Material or a New State of Matter: A Review and Reconsideration of the Aerogel. *Materials* **2013**, *6*, 941−968.

(13) Qian, F.; Troksa, A.; Fears, T. M.; Nielsen, M. H.; Nelson, A. J.; Baumann, T. F.; Kucheyev, S. O.; Han, T. Y.-J.; Bagge-Hansen, M. Gold Aerogel Monoliths with Tunable Ultralow Densities. *Nano Lett.* **2020**, *20*, 131−135.

(14) Qian, F.; Lan, P. C.; Freyman, M. C.; Chen, W.; Kou, T.; Olson, T. Y.; Zhu, C.; Worsley, M. A.; Duoss, E. B.; Spadaccini, C. M.; et al. Ultralight Conductive Silver Nanowire Aerogels. *Nano Lett.* **2017**, *17*, 7171−7176.

(15) Pierre, A. C.; Pajonk, G. M. Chemistry of Aerogels and Their Applications. *Chem. Rev.* **2002**, *102*, 4243−4266.

(16) Li, V. C.-F.; Dunn, C. K.; Zhang, Z.; Deng, Y.; Qi, H. J. Direct Ink Write (DIW) 3D Printed Cellulose Nanocrystal Aerogel Structures. *Sci. Rep.* **2017**, *7*, 8018.

(17) Maleki, H.; Shahbazi, M.-A.; Montes, S.; Hosseini, S. H.; Eskandari, M. R.; Zaunschirm, S.; Verwanger, T.; Mathur, S.; Milow, B.; Krammer, B.; et al. Mechanically Strong Silica-Silk Fibroin Bioaerogel: A Hybrid Scaffold with Ordered Honeycomb Micro-morphology and Multiscale Porosity for Bone Regeneration. *ACS Appl. Mater. Interfaces* **2019**, *11*, 17256−17269.

(18) Power, M.; Hosticka, B.; Black, E.; Daitch, C.; Norris, P. Aerogels as Biosensors: Viral Particle Detection by Bacteria Immobilized on Large Pore Aerogel. *J. Non. Cryst. Solids* **2001**, *285*, 303−308.

(19) Gao, B.; Wang, I.-W.; Ren, L.; Hu, J. Catalytic Methane Decomposition over Bimetallic Transition Metals Supported on Composite Aerogel. *Energy Fuels* **2019**, *33*, 9099−9106.

(20) Li, K.; Luo, Q.; Xu, J.; Li, K.; Zhang, W.; Liu, L.; Ma, J.; Zhang, H. A Novel Freeze-Drying-Free Strategy to Fabricate a Biobased Tough Aerogel for Separation of Oil/Water Mixtures. *J. Agric. Food Chem.* **2020**, *68*, 3779−3785.

(21) Randall, J. P.; Meador, M. A. B.; Jana, S. C. Tailoring Mechanical Properties of Aerogels for Aerospace Applications. *ACS Appl. Mater. Interfaces* **2011**, *3*, 613−626.

(22) Maleki, H.; Durães, L.; Costa, B. F. O.; Santos, R. F.; Portugal, A. Design of Multifunctional Magnetic Hybrid Silica Aerogels with Improved Properties. *Microporous Mesoporous Mater.* **2016**, *232*, 227−237.

(23) Heiligtag, F. J.; Airaghi Leccardi, M. J. I.; Erdem, D.; Süess, M. J.; Niederberger, M. Anisotropically Structured Magnetic Aerogel Monoliths. *Nanoscale* **2014**, *6*, 13213−13221.

(24) Jung, S. M.; Preston, D. J.; Jung, H. Y.; Deng, Z.; Wang, E. N.; Kong, J. Porous Cu Nanowire Aerosponges from One-Step Assembly and Their Applications in Heat Dissipation. *Adv. Mater.* **2016**, *28*, 1413−1419.

(25) Shi, D.; He, P.; Lian, J.; Chaud, X.; Bud'ko, S. L.; Beaugnon, E.; Wang, L. M.; Ewing, R. C.; Tournier, R. Magnetic Alignment of Carbon Nanofibers in Polymer Composites and Anisotropy of Mechanical Properties. *J. Appl. Phys.* **2005**, *97*, 064312.

(26) Feng, T.; Ye, X.; Zhao, Y.; Zhao, Z.; Hou, S.; Liang, N.; Zhao, L. Magnetic Silica Aerogels with High Efficiency for Selective Adsorption of Pyrethroid Insecticides in Juices and Tea Beverages. *New J. Chem.* **2019**, *43*, 5159−5166.

(27) Li, Y.; Liu, Q.; Hess, A. J.; Mi, S.; Liu, X.; Chen, Z.; Xie, Y.; Smalyukh, I. I. Programmable Ultralight Magnets via Orientational Arrangement of Ferromagnetic Nanoparticles within Aerogel Hosts. *ACS Nano* **2019**, *13*, 13875−13883.

(28) Faivre, D. Dry but Flexible Magnetic Materials. *Nat. Nanotechnol.* **2010**, *5*, 562−563.

(29) Olsson, R. T.; Azizi Samir, M. A. S.; Salazar-Alvarez, G.; Belova, L.; Ström, V.; Berglund, L. A.; Ikkala, O.; Nogués, J.; Gedde, U. W. Making Flexible Magnetic Aerogels and Stiff Magnetic Nanopaper Using Cellulose Nanofibrils as Templates. *Nat. Nanotechnol.* **2010**, *5*, 584−588.

(30) Yorov, K. E.; Shekunova, T. O.; Baranchikov, A. E.; Kopitsa, G. P.; Almásy, L.; Skogareva, L. S.; Kozik, V. V.; Malkova, A. N.; Lermontov, S. A.; Ivanov, V. K. First Rare-Earth Phosphate Aerogel: Sol−Gel Synthesis of Monolithic Ceric Hydrogen Phosphate Aerogel. *J. Sol-Gel Sci. Technol.* **2018**, *85*, 574−584.

(31) Janulevicius, M.; Klimkevicius, V.; Vanetsev, A.; Plausinaitiene, V.; Sakirzanovas, S.; Katelnikovas, A. Controlled Hydrothermal Synthesis, Morphological Design and Colloidal Stability of $GdPO_4 \cdot nH_2O$ Particles. *Mater. Today Commun.* **2020**, *23*, 100934.

(32) Wang, X.; Gao, M. A Facile Route for Preparing Rhabdophane Rare Earth Phosphate Nanorods. *J. Mater. Chem.* **2006**, *16*, 1360−1365.

(33) Yan, R.; Sun, X.; Wang, X.; Peng, Q.; Li, Y. Crystal Structures, Anisotropic Growth, and Optical Properties: Controlled Synthesis of Lanthanide Orthophosphate One-Dimensional Nanomaterials. *Chem.—Eur. J.* **2005**, *11*, 2183−2195.

(34) Wang, Z.; Shi, X.; Wang, X.; Zhu, Q.; Kim, B.-N.; Sun, X.; Li, J.-G. Breaking the Strong 1D Growth Habit to Yield Quasi-Equiaxed $REPO_4$ Nanocrystals (RE = La-Dy): Via Solvothermal Reaction and Investigation of Photoluminescence. *CrystEngComm* **2018**, *20*, 796−806.

(35) Yan, B.; Xiao, X. Hydrothermal Synthesis, Microstructure and Photoluminescence of Eu^{3+}-Doped Mixed Rare Earth Nano-Orthophosphates. *Nanoscale Res. Lett.* **2010**, *5*, 1962.

(36) Ding, M.; Chen, D.; Yin, S.; Ji, Z.; Zhong, J.; Ni, Y.; Lu, C.; Xu, Z. Simultaneous Morphology Manipulation and Upconversion Luminescence Enhancement of β-$NaYF_4$:Yb^{3+}/Er^{3+} Microcrystals by Simply Tuning the KF Dosage. *Sci. Rep.* **2015**, *5*, 12745.

(37) Heffernan, K. M.; Ross, N. L.; Spencer, E. C.; Boatner, L. A. The Structural Response of Gadolinium Phosphate to Pressure. *J. Solid State Chem.* **2016**, *241*, 180−186.

(38) Cho, J.; Kim, C. H. Solid-State Phase Transformation Mechanism from Hexagonal $GdPO_4$:Eu^{3+} Nanorods to Monoclinic Nanoparticles. *RSC Adv.* **2014**, *4*, 31385−31392.

(39) Zou, X.; He, L.; Tan, D.; Lei, F.; Jiang, N.; Zheng, Q.; Lin, D.; Xu, C.; Liu, Y. Anneal-Induced Transformation of Phase Structure, Morphology and Luminescence of $GdPO_4$:Sm^{3+} Nanomaterials Synthesized by a Hydrothermal Method. *Dalton Trans.* **2017**, *46*, 2948−2956.

(40) Wang, Z.; Li, J.-G.; Zhu, Q.; Ai, Z.; Li, X.; Sun, X.; Kim, B.-N.; Sakka, Y. EDTA-Assisted Phase Conversion Synthesis of $(Gd_{0.95}RE_{0.05})PO_4$ Nanowires (RE = Eu, Tb) and Investigation of Photoluminescence. *Sci. Technol. Adv. Mater.* **2017**, *18*, 447−457.

(41) Hernández, A. G.; Boyer, D.; Potdevin, A.; Chadeyron, G.; Murillo, A. G.; de J. Carrillo Romo, F.; Mahiou, R. Hydrothermal Synthesis of Lanthanide-Doped $GdPO_4$ Nanowires and Nanoparticles for Optical Applications. *Phys. Status Solidi A* **2014**, *211*, 498−503.

(42) Gschneidner, K. A., Jr.; Pecharsky, V. K.; Tsokol, A. O. Recent Developments in Magnetocaloric Materials. *Rep. Prog. Phys.* **2005**, *68*, 1479−1539.

(43) Wang, F. F. Y. Magnetic Susceptibilities of Gadolinium Orthophosphate ($GdPO_4$). *Phys. Status Solidi B* **1966**, *14*, 193−203.

(44) Kumar, G. A.; Balli, N. R.; Kailasnath, M.; Mimun, L. C.; Dannangoda, C.; Martirosyan, K. S.; Santhosh, C.; Sardar, D. K. Spectroscopic and Magnetic Properties of Neodymium Doped in $GdPO_4$ Sub-Micron-Stars Prepared by Solvothermal Method. *J. Alloys Compd.* **2016**, *672*, 668−673.

(45) Abécassis, B.; Lerouge, F.; Bouquet, F.; Kachbi, S.; Monteil, M.; Davidson, P. Aqueous Suspensions of $GdPO_4$ Nanorods: A Paramagnetic Mineral Liquid Crystal. *J. Phys. Chem. B* **2012**, *116*, 7590−7595.

(46) Du, Q.; Huang, Z.; Wu, Z.; Meng, X.; Yin, G.; Gao, F.; Wang, L. Facile Preparation and Bifunctional Imaging of Eu-Doped $GdPO_4$ Nanorods with MRI and Cellular Luminescence. *Dalton Trans.* **2015**, *44*, 3934−3940.

Supporting information

Ultralight Magnetic Nanofibrous GdPO₄ Aerogel

Matas Janulevicius[a], Vaidas Klimkevičius[a], Lina Mikoliunaite[a,b], Bonifacas Vengalis[b], Rokas Vargalis[a], Simas Sakirzanovas[a], Valentina Plausinaitiene[a], Albinas Zilinskas[a] and Arturas Katelnikovas[a,*]

[a] Institute of Chemistry, Vilnius University, Naugarduko 24, LT-03225 Vilnius, Lithuania
[b] Center for Physical Sciences and Technology, Saulėtekio al. 3, LT-10223 Vilnius, Lithuania

Email: arturas.katelnikovas@chf.vu.lt

S1. *GdPO$_4$ nanofiber preparation.*

During the typical synthesis procedure, a 0.5 mL of 0.8 mol/L Gd(NO$_3$)$_3$ stock solution was diluted to 20 mL using distilled water. Subsequently, 1.200 g (8 mmol) of tartaric acid was dissolved in 20 mL of distilled water, and added dropwise to Gd(NO$_3$)$_3$ solution. The obtained solution was stirred at room temperature for 30 min. in order to form solution A, containing Gd-tartaric acid complex. Then the pH of solution A was set to 7.0 by adding some ammonia solution. Afterwards, 0.046 g (0.4 mmol) of NH$_4$H$_2$PO$_4$ was dissolved in 20 mL of distilled water and the obtained solution was added dropwise to solution A under vigorous stirring, while maintaining pH value around 7 (by HNO$_3$ or ammonia solutions) and left stirring for 15 min. Then the volume of reaction mixture was increased to 80 mL by adding distilled water. Finally, the reaction mixture was poured into the Teflon bottle autoclave, which was sealed and placed into hydrothermal bomb, which was then placed into the oven for 12 h at 160 °C. After synthesis the obtained hydrogel was centrifuged at 500 rpm (using Centrifuge 5804 by Eppendorf), and washed with distilled water. This step was repeated 3 times. Subsequently, the obtained precipitate was diluted to 10 mL to produce a washed hydrogel. All the syntheses were repeated at least three times in order to evaluate the reproducibility of the obtained results.

S2. Instrumental setup

The frozen GdPO$_4$ hydrogel (containing GdPO$_4$ nanofibers) was freeze dried for 48 h in a *Labconco FreeZone 2.5* freeze-dryer operated at 0.010 mBar pressure and -82 °C temperature.

Powder XRD measurements were carried out using parallel beam geometry on a Bruker D8 Advance da Vinci design diffractometer (LynxEye detector and Cu Kα radiation). The diffraction patterns were analyzed using Topas (Bruker AXS) software (version 4.2) according to Le Bail decomposition procedure.

SEM images were taken with high-resolution scanning electron microscope (FE SEM) Hitachi SU-70, with accelerating voltage up to 10 kV. Samples for SEM were prepared by ultrasonically dispersing aerogel in distilled water and adding 20 μL of aqueous dispersion on a Si plate.

TEM imaging was performed using FEI Tecnai F20 X-TWIN transmission electron microscope. Measurements were carried out using 200 kV accelerating voltage, images were obtained using Gatan Orius CCD camera.

The surface area was determined by conducting nitrogen adsorption measurements using a Micromeretics ASAP 2020 (Brunauer−Emmett−Teller method) device.

Magnetic properties were evaluated by encapsulating a fixed amount of rod-like $GdPO_4$ nanocrystals compactly into a Teflon tube with the inner diameter of 2.0 mm to increase density of the investigated material and to reduce possible displacement of the nanocrystals under an applied magnetic field. The real part of differential (AC) magnetic susceptibility of the sample, $\chi(H)$, was measured at a fixed frequency (f = 31.5 kHz) by using AC susceptometer by applying DC magnetic field, H, ranging from -1.0 to 1.0 T and small AC field ($h \sim 10^{-4}$ T) oriented parallel to the applied field H. Coil system of the susceptometer consisted of magnetically coupled primary and secondary coils. The pick up coil consisted of two identical sections wounded in opposite directions and connected in series to make the output signal in the absence of the sample equal to zero. The $M(H)$ curves were obtained numerically by integrating the $\chi(H)$ curves. The measurement equipment has been calibrated by using samples with certified magnetic properties.
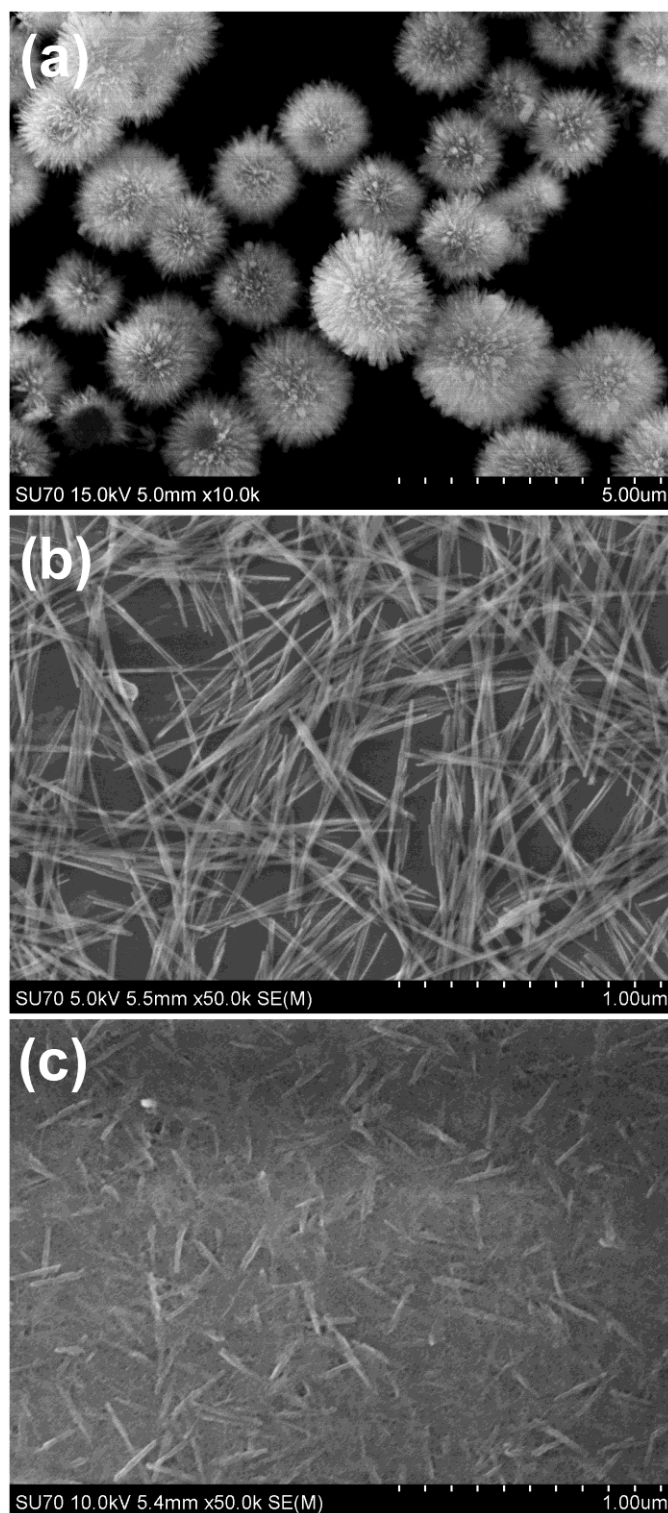
Figure S1. SEM images of GdPO₄ particles obtained under different conditions: (a) pH = 2 (without stirring), (b) pH = 10 (without stirring), and (b) pH = 10 (with stirring).
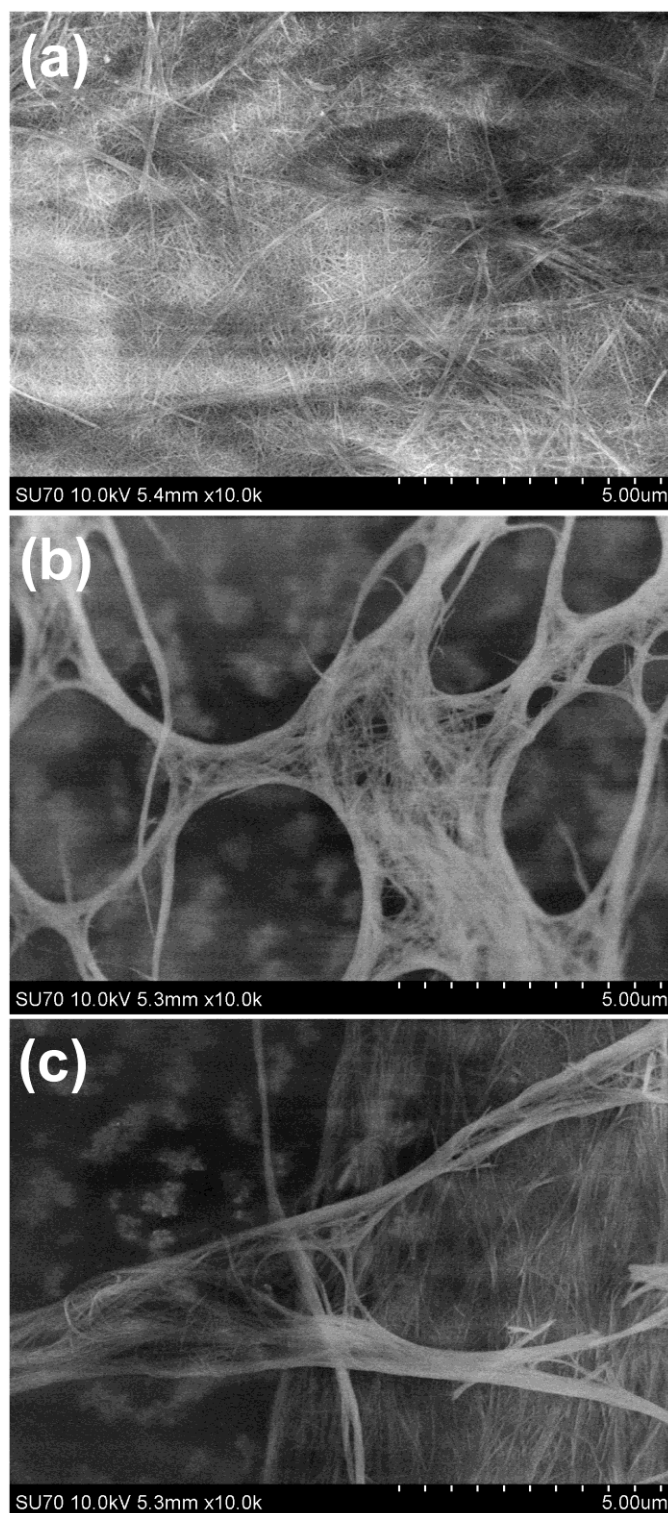
Figure S2. Low resolution SEM images of aerogels obtained after freeze-drying 10 mL (a), 20 mL (b), and 30 mL (c) hydrogel.
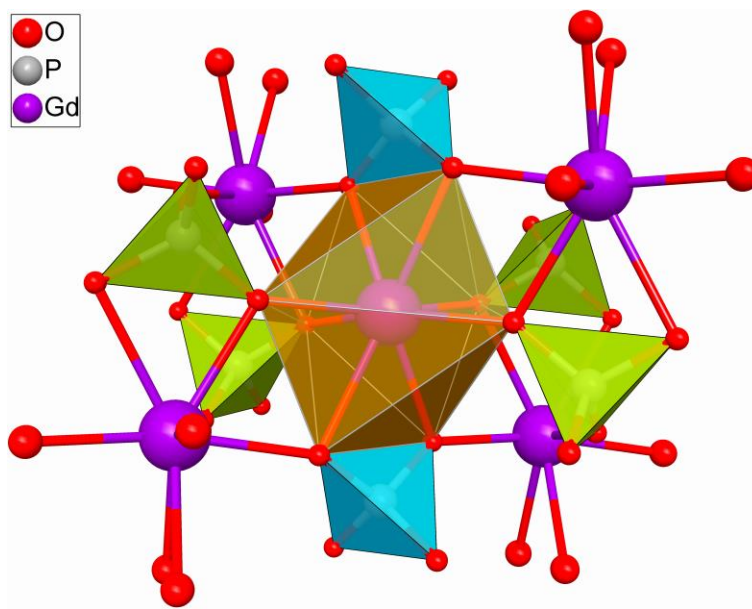
Figure S3. Building block in trigonal rhabdophane $GdPO_4 \cdot H_2O$ structure. Cyan and green tetrahedra show edge and vertex sharing PO_4, respectively.
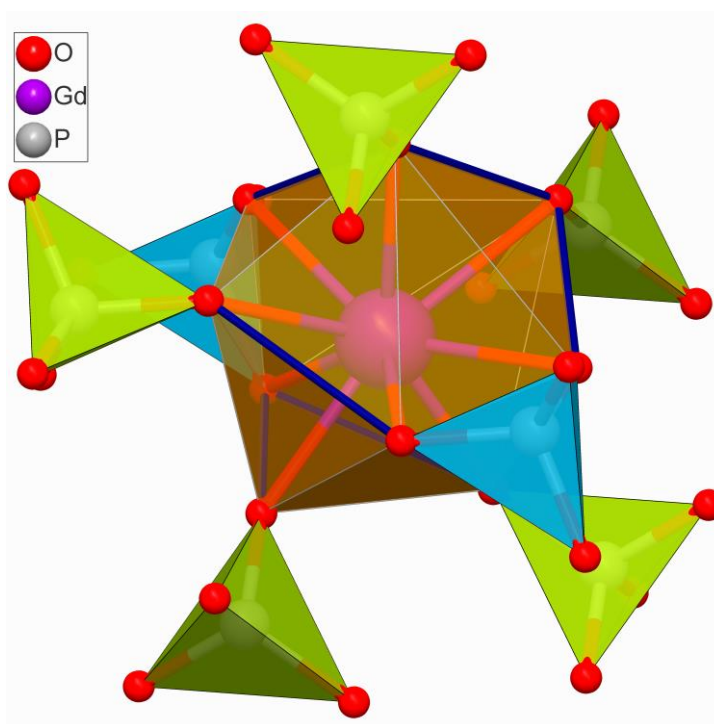
Figure S4. Building block in monoclinic monazite $GdPO_4$ structure. Cyan and green tetrahedra show edge and vertex sharing PO_4, respectively. The edges of GdO_9 polyhedron, that are shared with other six GdO_9 polyhedrons, are marked in blue.
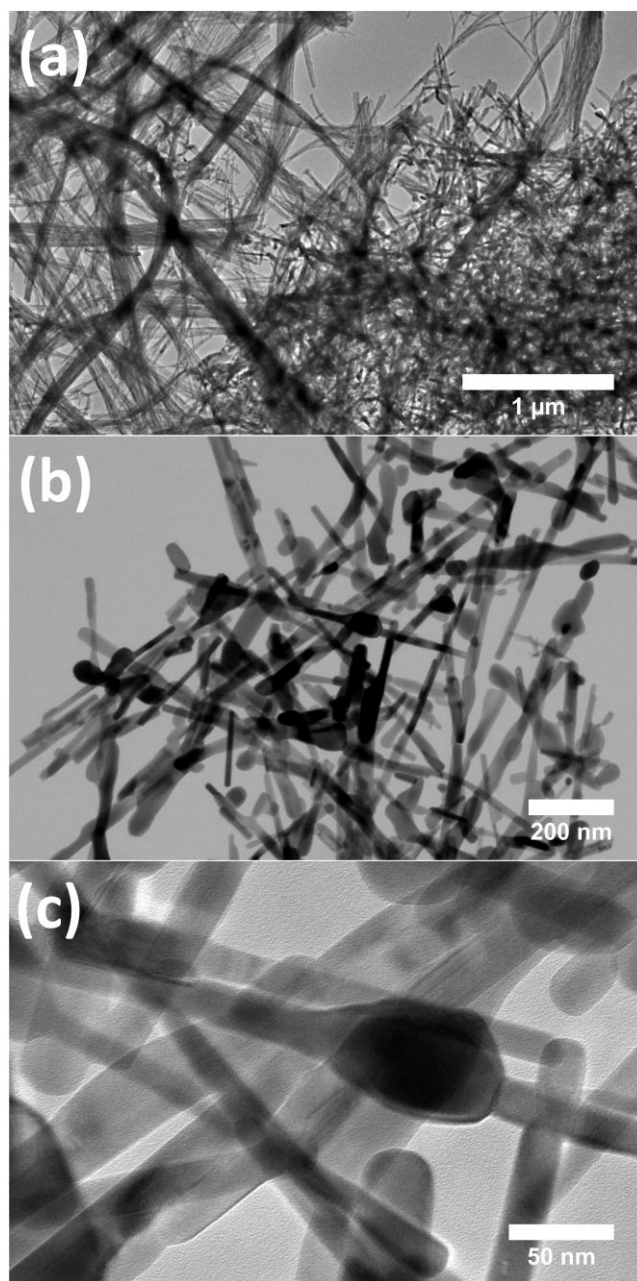
Figure S5. TEM images of monoclinic GdPO$_4$ indicating signs of melting (a-c).
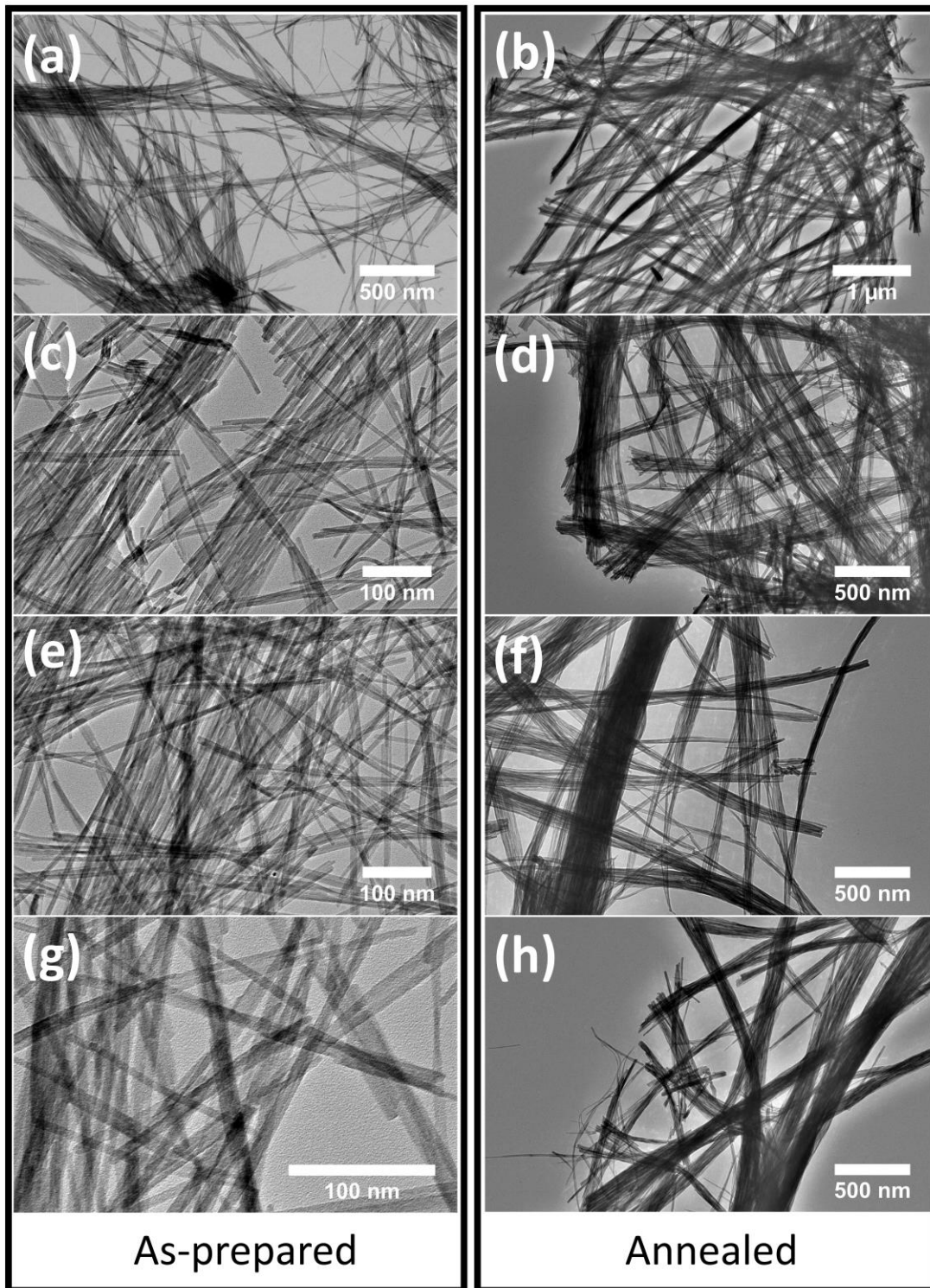
Figure S6. TEM images of as-prepared (a, c, e, g) and annealed (b, d, f, h) GdPO$_4$ aerogel samples.